JOURNAL OF OPTOELECTRONICS AND ADVANCED MATERIALS Vol. 16, No. 9-10, September - October 2014, p. 1071 - 1082

XBn and cascade infrared detectors for mid-wave range and HOT conditions

P. MARTYNIUK[a*], W. GAWRON[a], A. KOWALEWSKI[a], E. PLIS[b], S. KRISHNA[b], A. ROGALSKI[a]
[a]Institute of Applied Physics, Military University of Technology, 2 Kaliskiego Str., 00-908 Warsaw, Poland
[b]Department of Electrical and Computer Engineering, Center for High Technology Materials, University of New Mexico, Albuquerque, New Mexico 87106, USA

Unlike thermal detectors, infrared photon detectors normally operate at cryogenic temperatures to suppress the noise coming from mechanisms associated with the inherited capability of the narrow band gap materials. The potential applications of the infrared detectors require systems with low cost, size, weight, power consumption and what is the most important, high operating temperature condition. The very first attempts to reach high operating temperature conditions were concentrated on photoconductors and photoelectromagnetic detectors. Next, non-equilibrium detector design with Auger suppression and optical immersion were introduced. Currently, a new approach related to barrier structures and interband cascade infrared devices has been successfully put into practice. Among the high operating temperature materials the following should be enumerated: HgCdTe, InAsSb, and type-II InAs/GaSb superlattices. The paper presents recent strategies: barrier and cascade structures to increase performance at high operation temperature conditions.

(Received December 06, 2013; accepted September 11, 2014)

Keywords: HOT, BIRD, XBn, IB CID, T2SLs InAs/GaSb, HgCdTe, InAsSb

1. Introduction

Hitherto, a number of concepts to improve the mid-wave (MWIR) infrared photodetector performance reaching the high operating temperature (HOT) conditions have been introduced and successfully implemented [1]. Historically, among the HOT technologies there must be listed: photoelectromagnetic detectors (PEM), magnetoconcentration and Dember effect detectors [2,3]. Next, significant increase of operating temperature without lowering the performance of the detector was achieved by implementation of the non-equilibrium conditions to suppress an Auger generation recombination (GR) process [4,5]. Additionally, Auger GR could be limited by designing the detectors with materials inherently exhibiting lower Auger GR rates. Here, the InAs/GaSb type-II superllatices (T2SLs; SL-superllatice) should be enumerated. Theoretical predictions pointed out on quantum dot infrared detectors (QDIPs) potential HOT capability but technological problems related to the self-organised growth of uniform QDs layers have impeded the development of this type of detectors [6].

The Shockley-Read-Hall (SRH) GR contribution may be efficiently restricted by the barrier's incorporation to the detector structure [7]. The detectors, combining both: barrier infrared detector's (BIRD) architecture to include "W" (InAs/GaInSb/InAs/AlGaInSb), "M" (GaSb/InAs/GaSb/AlSb) and presented recently "N" (AlSb/GaSb/InAs) either barrier or active layer designs improving absorption efficiency, complementary barrier structures (CBIRD) have been reported already showing potential HOT conditions in MWIR range [8−11].

The key requirement which must be met to construct the BIRD structure is "zero" band offset either in conduction or valence band depending on assumed carrier type which is to be blocked (nBn or pBp) [12]. The most promising and currently popular are T2SLs InAs/GaSb and InAsSb/B-AlAsSb nBn structures (B stands for the barrier) [13]. The physical properties underlay a potential T2SLs' advantage over bulk materials, however there are many indicators stressing on low quantum efficiency (20−30% in MWIR range) and short minority carrier lifetimes [14,15].

The BIRD architecture has been implemented into HgCdTe, where theoretical predictions and technological attempts show a prospect for the circumventing of the p-type doping requirements in MBE technology [16].

Recently, even higher than room temperature operation conditions has been reached by T2SLs InAs/GaSb interband cascade infrared detectors (IB CID) introduced to increase the absorption efficiency [17].

The paper focuses on development of IR HOT detectors. The potential approaches related to materials, barrier T2SLs InAs/GaSb, InAsSb/B-AlAsSb, HgCdTe/B-HgCdTe, T2SLs InAs/GaSb and T2SLs InAs/GaSb IB CID detectors that eliminate the cooling requirements of IR photodetectors operating in MWIR range are presented.

2. BIRD structures

The unipolar barrier infrared detector (UBIRD) design modifies the architecture of the detector in comparison to the traditional p-n homojunction detectors. Theoretically, thanks to introducing of the wide gap material with the respect to the surrounding materials, the UBIRD detector blocks one carrier type and allows unimpeded flow of the other [18]. The simplest example of the BIRD XBn is nBn structure consisting of n-type absorber (active layer-AL); n-type wide gap barrier layer (BL) and n-type contact layer (CL). The nBn band gap diagram compared to the traditional p-n homojunction is shown in Fig. 1 (a) and (c) respectively.

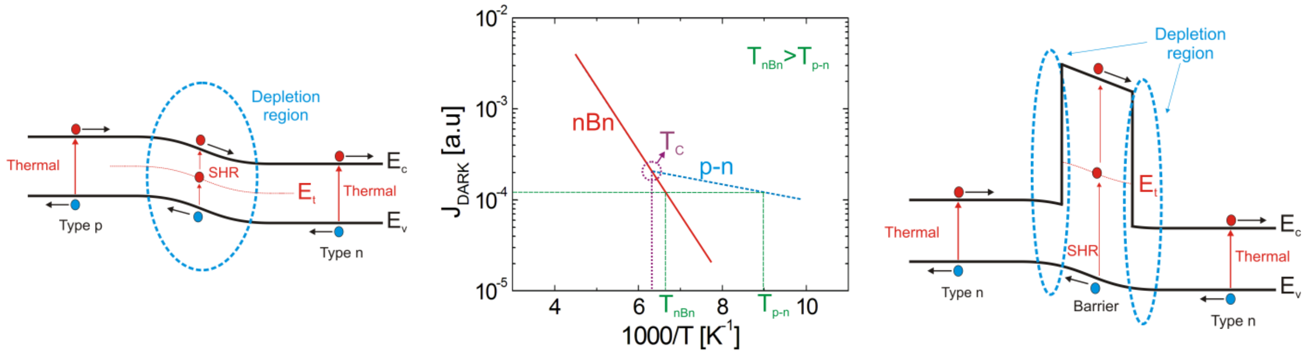

(a) *(b)* *(c)*

Fig. 1. Band gap diagram of p-n photodiode (a); Arrhenius plot of the dark current in standard p-n photodiode (dashed line) and nBn (solid line) barrier detector (b); band gap diagram of nBn barrier detector (c).

Aside from blocking of the majority carriers, nBn structure efficiently suppresses the SRH GR (due to the reduction of depletion region within the active layer), and reduces leakage currents. Fig. 1 (b) presents Arrhenius plot of the dark current in a conventional photodiode and nBn structure. T_C stands for the crossover temperature at which the diffusion and GR contributions are at equilibrium. Fig. 1 (b) clearly indicates that nBn detetctor exhibits a higher signal-to-noise ratio and allow higher operating temperature $T_{nBn} > T_{p-n}$ in comparison to traditional p-n photodiode.

The detector surface conductivity and AL doping determine the type of the barrier which must be implemented. In addition, the proper location of the barrier within the structure is crucial to ensure that photogenerated carriers are not blocked by the barrier layer. The barrier should be located near the minority carrier collector and away from the region of optical absorption. For material systems in configuration absorber/barrier, where a large conduction band offset is not achievable (e.g. HgCdTe/B-HgCdTe), the pBn (with p-type CL) architecture may be preferable to limit the electron transport resulting from thermionic emission over the barrier. In addition, the traditional nBn structure requires voltage to operate (the collection efficiency of the detector with high valence band offset could be overcome by applying large reverse bias to the detector architecture). Once zero bias operation is crucial, the structure with p-type CL may be used (pBn architecture).

The large band offset requirement in one band and zero offset in the other is not the only one obligation to fabricate XBn BIRD detector. The lattice-matching between surrounding materials is significant and very stringent to reach.

2.1 Materials for BIRD detectors

Currently among the XBn materials, 6.1 Å compound family plays decisive role (lattice-matching between surrounding materials is significant). The 6.1 Å material system offers high performance linked with enormous design flexibility, direct energy gaps and strong optical absorption. Additionally, these material systems have constituents with type I, II and III band alignments as presented in Fig. 2 (a). The most popular is InAs with barrier $AlAs_ySb_{1-y}$. The theoretical simulation suggests barrier composition in the $0.14 < y < 0.18$, where valence band offset (VBO) should be less than $3k_BT$ and having no impact on detector's performance [19]. The second material system is $InAs_{1-x}Sb_x$ with barrier $AlAs_ySb_{1-y}$ grown on GaAs and GaSb substrates (see Fig. 2 (b)) [20]. The HgCdTe/B-HgCdTe nBn devices operating in MWIR range were presented by Itsuno *et al.* [21].

HgCdTe is a close to ideal infrared detector material system. Its unique position depends on following physical properties being direct consequence of the energy band structure of this zinc-blende semiconductor:

a) composition-dependent tailorable band gap;

b) large optical coefficients, high quantum efficiency;

c) favourable inherent recombination mechanisms leading to long carrier lifetime and high operating temperature.

Moreover, additional specific advantages of HgCdTe are: the ability to obtain both low and high carrier concentrations, high mobility of electrons, and low dielectric constant. The extremely small change of lattice constant with composition makes it possible to grow high quality layered and graded gap structures. In the case of HgCdTe HOT devices, a moderate p-type doping of the absorber detector region is widely used for suppression of the Auger mechanisms. More efficient suppression can be obtained with non-equilibrium depletion of the semiconductor.

Interest in T2SLs InAs/GaSb in MWIR range is not only related to an advanced $A^{III}B^{V}$ molecular beam epitaxial (MBE) growth of these structures, but also with distinctive capability of the new artificial material with totally different physical properties in comparison to InAs and GaSb layers. Electronic properties of SLs are considered to be superior to those of the InAsSb and HgCdTe alloys. The effective masses are not directly dependent on the band gap energy comparing to bulk semiconductor.

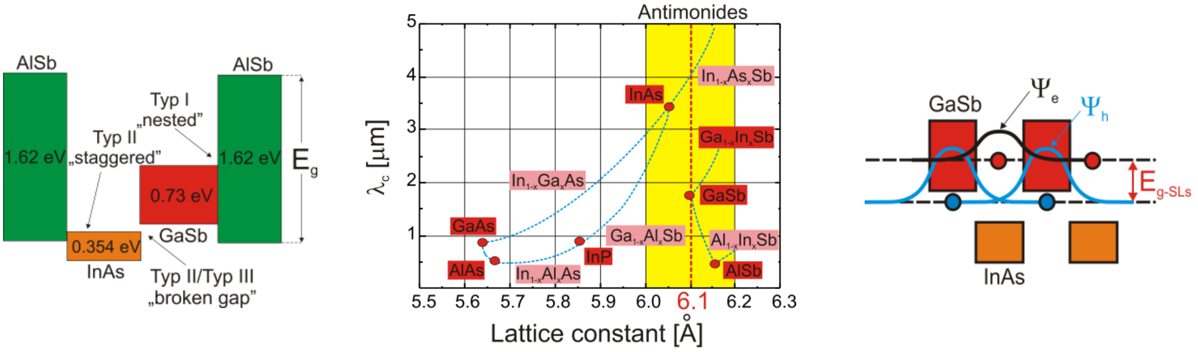

(a) (b) (c)

Fig. 2. The relative energy alignments of 6.1 Å material family (a); antimonides from 6.1 Å material family (b); wawefunction overlapping in T2SLs InAs/GaSb (c).

The electron effective mass of InAs/GaSb SL is larger ($m^*/m_o \approx 0.02–0.03$, compared to $m^*/m_o = 0.009$ in HgCdTe with the same band gap $E_g \approx 0.1$ eV) reducing tunneling currents in the SL in comparison to the HgCdTe. Due to spatial separations of electrons and holes, the Auger recombination rates in T2SLs are suppressed by several orders of magnitude, compared to those of bulk HgCdTe/InAsSb with similar bandgap. Although in-plane mobilities drop precipitously for thin wells, electron mobility ~ 10^4 cm^2/Vs have been observed in T2SLs InAs/GaSb superlattices with the layers less than 40 Å. While mobility in these SLs are found to be limited by the same interface roughness scattering mechanism, detailed band structure calculations reveal a much weaker dependence on layer thickness, in rational agreement with experiment. In the case of InAs/GaSb SLs structures the absorption is strong for normal incidence of light. Consequently, the SL structures should provide high responsivity, as already reached with HgCdTe, without any need for gratings (unlike to quantum well infrared photodetectors-QWIPs). There is a nearly zero VBO between T2SLs InAs/GaSb (e.g. 10 ML InAs/10ML GaSb) and $Al_{0.2}Ga_{0.8}Sb$ which favours these two materials for XBn structures. Even though potential superiority over bulk materials and different active layer architectures increasing electron-hole wavefunction overlapping ("W", "M", "N"-refer to the relative energy alignment of 6.1 Å family presented in Fig. 2 (a) and wavefunction overlapping shown in Fig. 2. (c)) there are many signs stressing technological problems with uniformity and proper width of SLs resulting in low quantum efficiency. The problems with low level of quantum efficiency in T2SLs InAs/GaSb could be overcome by using of T2SLs InAs/InGaSb. Indium introducing to SLs structure increases the optical matrix element [22−24].

For the applications where the cut-off wavelengths shorter than 4.2 μm are needed, it is advisable to use InAsPSb/B-AlAsSb architecture exhibiting relatively long minority carrier lifetimes in comparison to the T2SLs InAs/GaSb being limited by short SRH lifetimes [25].

2.2 HgCdTe/B-HgCdTe and InAsSb/B-AlAsSb XBn detectors modeling

XBn InAsSb and HgCdTe detectors (with n/p-type CL) were simulated with Apsys platform by Crosslight Inc. The numerical simulations included: radiative (RAD), Auger, SRH GR and both: trap-assisted tunnelling (TAT) and band-to-band (BTB) at barrier layer/absorber heterojunction. Since the both HgCdTe and AlAsSb barrier height in conduction band was estimated to be within the range of ~ 0.4–2 eV, the SRH GR mechanism in the AlAsSb barrier region is unimportant in assessing the InAsSb/B-AlAsSb XBn performance, while in HgCdTe/B-HgCdTe SRH GR contribution is evident in HOT conditions.

The XBn detector requires that the valence bands of the three constituent layers line up closely to allow minority carrier transport between the absorber and contact layers, and this requirement has so far restricted applications to the materials presented above. The electron affinity of both barrier layer and absorber layer seems to be the most decisive parameter to choose in XBn structures modeling. The simulation parameters were presented in Tables 1 and 2.

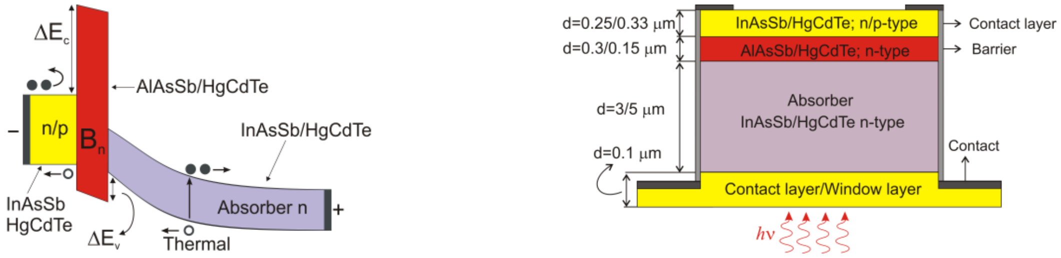

(a) *(b)*

Fig. 3. Energy band diagram of the simulated nBn photodetector under reverse bias conditions (a); modelled nBn structure (b).

The detailed description of the simulation procedure and results related to the nBn detectors may be found in our previous papers [26,27] and implemented to pBn detector's simulation. The both InAsSb/B-AlAsSb and HgCdTe/B-HgCdTe XBn MWIR structures modelled in this paper are shown in Fig. 3 (a) and (b) respectively. Structure consists of n-type 3(5)-μm thick InAsb (HgCdTe) absorber layer doped to the level of N_D = 5×10^{15}(10^{14}) cm^{-3}. After the AL, an n-type AlAsSb/HgCdTe barrier layer was grown with a thickness of 0.3 (0.15) μm, (AlAsSb y = 0.09; HgCdTe graded x = 033→0.6→0.275) and doping N_D = 10^{16} (2×10^{15}) cm^{-3}. The BL thickness was assumed to prevent electron tunnelling between the top CL and the AL layers therefore, the majority current is blocked by the barrier material under reverse bias.

Table 1. Parameters taken in modeling of MWIR XBn InAsSb/AlAsSb detectors.

	Contact/Cap Layer (CL)	Barrier (BL)	Absorber (AL)	Contact layer (CL)
Doping, N_D/N_A [cm^{-3}]	$10^{14}\rightarrow10^{17}$	10^{16}	5×10^{15}	5×10^{17}
Doping Gauss tail, dx [μm]	0.05	0.05	0.05	0.02
Composition, x/y	0.09	0.08	0.09	0.09
Geometry, d [μm]	0.25	0.3	3	0.1
Electrical area, A [μm^2]	200×200			
Overlap matrix, F_1F_2	0.3	Auger coefficients: $C_n = C_p = 10^{-27}$ cm^6/s	0.3	0.3
Trap energy level, E_{Trap}	0.25×E$_g$	0.5×E$_g$	0.25×E$_g$	0.25×E$_g$
Trap concentration, N_{Trap} [cm^{-3}]	10^9	10^4	10^9	10^9
Minority carrier lifetime SRH, τ_n,	50; 0.5	50; 0.5	50; 0.5	50; 0.5
Electron affinity [eV]	$5.72-0.31x$	$3.65-0.15x$	$5.72-0.31x$	$5.72-0.31x$
Incident power density, Φ [W/m^2]	500			

Table 2. Parameters taken in modeling of MWIR XBn HgCdTe detectors.

	Contact/Cap Layer (CL)	Barrier (BL)	Absorber (AL)
Doping, N_D/N_A [cm^{-3}]	$10^{14}\rightarrow10^{17}$	5×10^{15}	10^{14}
Doping Gauss tail, dx [μm]	0.05	0.05	0.02
Composition, x/y	0.33	0.33→0.6→0.275	0.275
Geometry, d [μm]	0.16	0.15	5
Electrical area, A [μm^2]	120×120		
Overlap matrix, F_1F_2	0.2		
Trap energy level, E_{Trap}	0.5×E$_g$		
Trap concentration, N_{Trap} [cm^{-3}]	10^9	10^4	10^9
Minority carrier lifetime SRH, τ_n, τ_p [μs]	10; 1		
Electron affinity [eV]	$4.23-0.813[E_g(x,T)-0.083]$		
Incident power density, Φ [W/m^2]	500		

As mentioned, band gap engineering reduces SRH GR rate in the depletion region at BL suppressing net current by controlling single ca rrier flow: $J_{DARK} \propto \exp\left(-E_g/2k_BT\right)$. Having taken this into consideration, SRH GR rate, $\left|R_{SRH}\right|$ is reduced when the depletion region is excluded from the active layer. This requirement is fulfilled if barrier and absorber are n (or p) type doped. Once barrier or absorber layer have the opposite doping type, wider depletion region develops increasing GR rate and potentially decreasing detector performance. Fig. 4 presents $|R_{SRH}|$ rate calculated for the p-n junction and XBn structures at T = 300 K, V = 400 mV and 500 mV corresponding to “turn-on” voltages for HgCdTe/B-HgCdTe and InAsSb/B-AlAsSb material system, respectively. Incorporation of the wide gap barrier reduces $|R_{SRH}|$ by five orders of magnitude in comparison to the p-n (x = 0.275) junction for HgCdTe, while for InAsSb/B-AlAsSb due the much higher conduction band offset the $|R_{SRH}|$ drops more significantly.

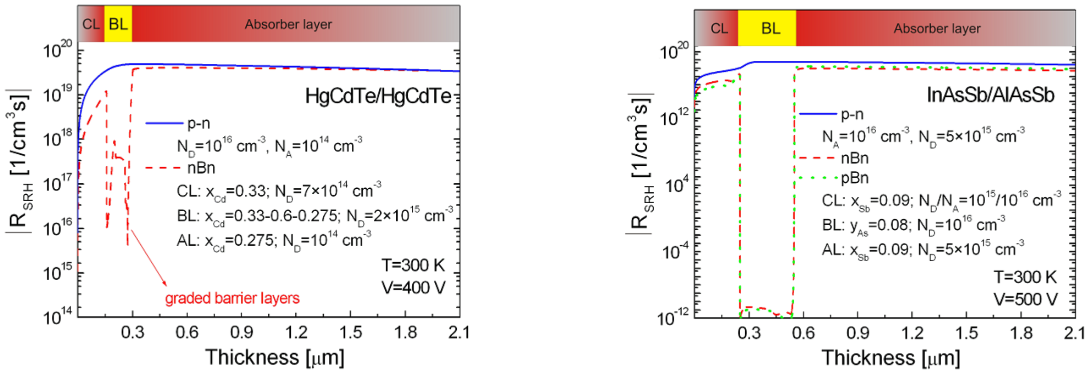

(a) (b)

Fig. 4. $|R_{SRH}|$ *for p-n and XBn HgCdTe/B-HgCdTe (a) and InAsSb/B-AlAsSb (b) detectors.*

The calculated energy band diagrams for XBn detector for unbiased structures are depicted in Fig. 5 (a)−(c) respectively. The XBn type detector should be reversely biased (i.e. positive voltage applied to the absorber contact). The proper type of doping of the CL influences the ΔE_v allowing nearly unimpeded flow of the holes to the contact layer. For the same level of doping of the contact layer $N_A = N_D = 10^{17}$ cm^{-3} the barrier height at the BL and AL heterojunction decreases more than four times reducing “turn-on” voltage for pBn architecture and allowing nearly “zero-bias” operating conditions in comparison with nBn InAsSb/B-AlAsSb detector. At the same time ΔE_c is slightly higher for pBn (ΔE_c = 2050 meV) in comparison to n-type CL (ΔE_c = 1970 meV).

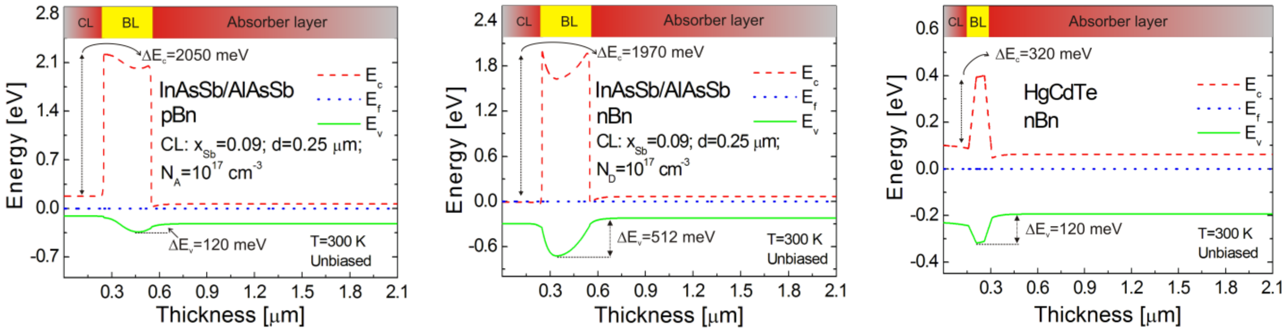

(a) (b) (c)

Fig. 5. Simulated energy band structures for XBn HgCdTe/B-HgCdTe and InAsSb/B-AlAsSb for unbiased conditions.

Comparison of the energy band alignment between unbiased and biased conditions directly indicates that XBn detectors require a proper level of voltage being applied to the detector to align the valence bands (at barrier-absorber interfaces). The p-type CL allows operation much more below the “turn-on” voltage level estimated for n-type CL. Figures 6 (a) and (b) present the cap-barrier (ΔE_c) and barrier-absorber (ΔE_v) barrier heights versus applied voltage for T = 300 K, respectively. It is clearly visible that applying the V = 500 mV to the nBn InAsSb/B-AlAsSb structure, the energy barrier for holes is being reduced by more than three times (from 270 to 80 meV) in comparison to the equilibrium conditions. The minority carriers in XBn architecture are effectively blocked for the ΔE_v > 78 meV at T = 300 K, while below VBO should not have any influence on the carrier transport. It is shown that applied voltage mostly influences ΔE_v, while ΔE_c keeps nearly constant value (e.g. for barrier-absorber interface $\Delta E_v \approx 270 \rightarrow 4$ meV and cap-barrier interface $\Delta E_c \approx 2038 \rightarrow 2032$ meV for $V = 0 \rightarrow 1$V, respectively for nBn InAsSb/B-AlAsSb). The condition of unimpeded minority carrier transport to the CL (ΔE_v < 78 meV) is met for V > 500 mV, while for nBn HgCdTe detector is much lower reaching V = 150 mV. The voltage contribution is much more visible and distinguishable for HgCdTe/B-HgCdTe nBn detector within analyzed bias range, while above V > 400 mV both ΔE_v and ΔE_c keep almost constant values ($\Delta E_v \approx 35$ meV; $\Delta E_c \approx 235$ meV).

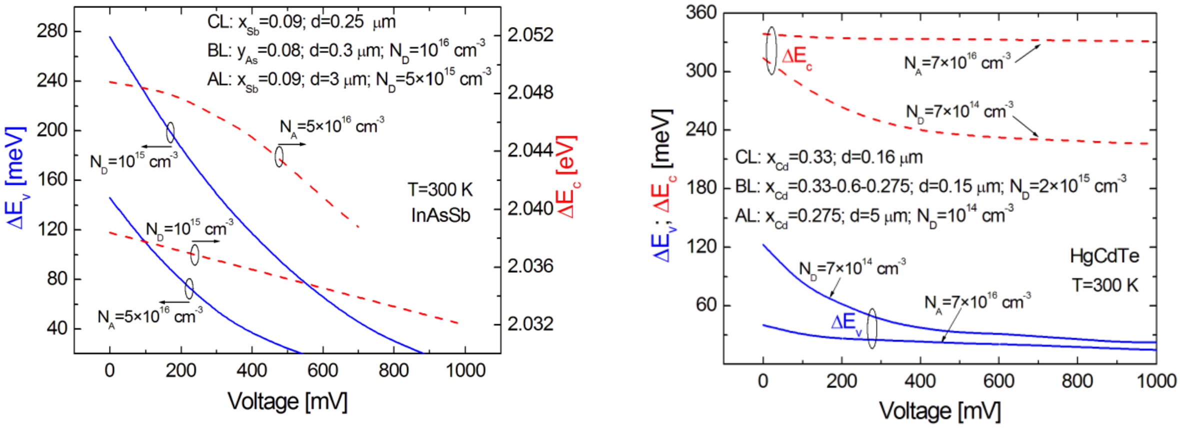

(a) *(b)*

Fig. 6. ΔE_c and ΔE_v for cap-barrier and barrier-absorber interfaces versus applied voltage for XBn detectors for selected CL doping.

Fig. 7 (a) presents dark current characteristics versus inverse temperature for both XBn and p-n $InAs_{0.91}Sb_{0.09}$. In the case of InAsSb XBn structures the simulations were performed for the following CL doping $N_D = N_A = 10^{15}$; 10^{17} cm^{-3}, while the voltage was assumed to be at the level of "turn-on" bias (V = 500 mV). In the case of p-n $InAs_{0.91}Sb_{0.09}$ photodiode, the J_{DARK} characteristic exhibits two slope behaviour, where the both diffusion and GR contributions within analyzed temperature range could be distinguished, while nBn detector exhibits characteristic one slope behaviour (diffusion contribution) for both analyzed CL doping $N_D = 10^{15}$; 10^{17} cm^{-3}. Increasing the CL doping $N_D = 5\times10^{15}\rightarrow10^{17}$ cm^{-3}, J_{DARK} decreases nearly by two orders of magnitude due to the fact that both ΔE_c and ΔE_v increases to the level: 1970→2038 meV and 275→512 meV, respectively. The simulation results are compared to the measured ones which could be fitted by the relation: $\propto T^r \exp\left(-qE_{Diff}/k_BT\right)$, where E_{Diff} represents the AL's band gap energy at T = 0 K. The proper agreement between simulation and experimental results were found for $r \approx 3$ and $E_{Diff} \approx 340$ meV. The GR contribution could be expressed by the same formula assuming $E_{GR} \approx E_{Diff}/2$ and $r \approx 1.5$. The GR contribution to the net J_{DARK} in the photodiode dominates below T_C, while above this temperature the diffusion contribution plays decisive role. Comparing dark currents of the barrier detector and p-n photodiode, having the same AL's geometry and doping, indicates that XBn structure may surpass photodiode's performances close to the T_C. The saturation current in photodiode could be expressed by the formula (1) and taking into consideration the fact that BIRD architecture is a minority carrier device, even in diffusion mode XBn structures should exhibit slightly lower dark current in comparison to the traditional p-n detectors:

$$J_s = \left(k_BT\right)^{0.5} n_i^2 q^{0.5}\left[\frac{1}{p_{po}}\left(\frac{\mu_e}{\tau_e}\right)^{0.5} + \frac{1}{n_{no}}\left(\frac{\mu_h}{\tau_h}\right)^{0.5}\right]^{-1} \qquad (1)$$

where n_i is a intrinsic concentration, p_{po} and n_{no} are majority carrier concentration, μ_e and μ_h are carrier mobility, τ_e and τ_h are electron and hole lifetimes in p-type and n-type regions, respectively.

Once the p-type CL doping is in the level of $N_A = 10^{15}$ cm^{-3}, the pBn J_{DARK} characteristics correspond to that presented for nBn with the comparable CL n-type doping $N_D = 10^{15}$ cm^{-3}. Increasing the p-type doping of the CL again two slope behaviour is observed (for V = 500 mV). Diffusion contribution dominates above $T > 256$ K, while below GR and tunnelling mechanism plays a decisive rule. It is evident that both: nBn and pBn InAsSb/AlAsSb detectors reaches comparable dark currents above > 256 K. Unlike for high p-type CL doping in pBn structures, nBn InAsSb/B-AlAsSb J_{DARK} characteristics are strongly temperature dependent in analyzed "turn-on" voltage level.

Similar considerations were performed for HgCdTe XBn detectors (see Fig. 7 (b)). The both BTB and TAT mechanisms were found to be negligible at the BL and AL heterojunction. The simulation results were compared to those presented by Itsuno *et al.* (V = 800 mV, n-type CL's doping $N_D = 7\times10^{14}$ cm^{-3}) showing proper agreement. The nBn HgCdTe/B-HgCdTe structures for two analyzed CL doping (7×10^{14};10^{16} cm^{-3}) exhibit one slope behaviour. In this case the influence of SRH GR mechanism is more evident ($\Delta E_c \approx 350$ meV). The experimental data could be fit by relation: $\propto T^{1.5}\exp\left(-q0.091/k_BT\right)$, where 0.091eV corresponds to $E_g/2$ at T = 300 K for x = 0.275. CBIRD architecture reduces dark current nearly 100 times depending on temperature.

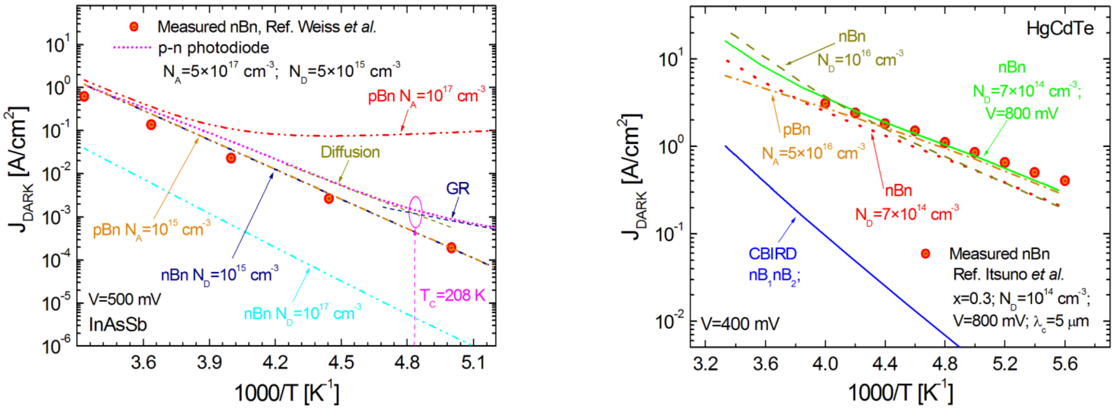

(a) *(b)*

Fig. 7. J_{DARK} versus inverse temperature for nBn/pBn InAsSb/AlAsSb (a); nBn/pBn HgCdTe/B-HgCdTe and CBIRD (b) detectors for selected voltages. The experimental results were taken after Weiss et al. [20] and Itsuno et al. [21].

The barrier's influence is clearly evident in Fig. 8 (a) and (b) respectively, where J_{DARK} versus voltage characteristics are shown for nBn structures over the temperature range 250−300 K in increments of 25 K. The "turn-on" voltage, is assumed to be V = 500 mV and 400 meV for InAsSb/B-AlAsSb and HgCdTe/B-HgCdTe, respectively. In the considered temperature range three distinct regions may be distinguished. For InAsSb/B-AlAsSb detector (see Fig. 8 (a)) and reverse biases between 0 and 50 mV, J_{DARK} is extremely sensitive to bias, while in range from 50 to 500 mV, J_{DARK} is less voltage dependent. As mentioned above, ΔE_v for V = 500 mV is comparable with 78 meV, which means that holes are nearly freely transported to the CL giving contribution to the net J_{DARK}. It is shown, that for reverse voltages $V < 500$ mV the dark current increases sharply, while above $V >$ 500 mV slight increase of the current versus bias is observed. In simulated voltage range there is no tunnelling contribution which is mainly caused by the fact that the barrier structure is diffusion limited reaching HOT conditions. The J_{DARK} characteristics at each simulated temperature exhibit a current plateau above 500 mV, while below, voltage sensitive region is observed. In addition the valence band barrier layer was incorporated between AL and + contact which effectively limits the hole injection to the absorber layer. For HgCdTe/B-HgCdTe (see Fig. 8 (b)) nBn, again three distinct regions could be distinguished. It must be stressed that J_{DARK} slightly increases with applied voltage due to the fact that in HgCdTe modeling, n$^+$ contact layer was not implemented to restrict hole injection from the contact.

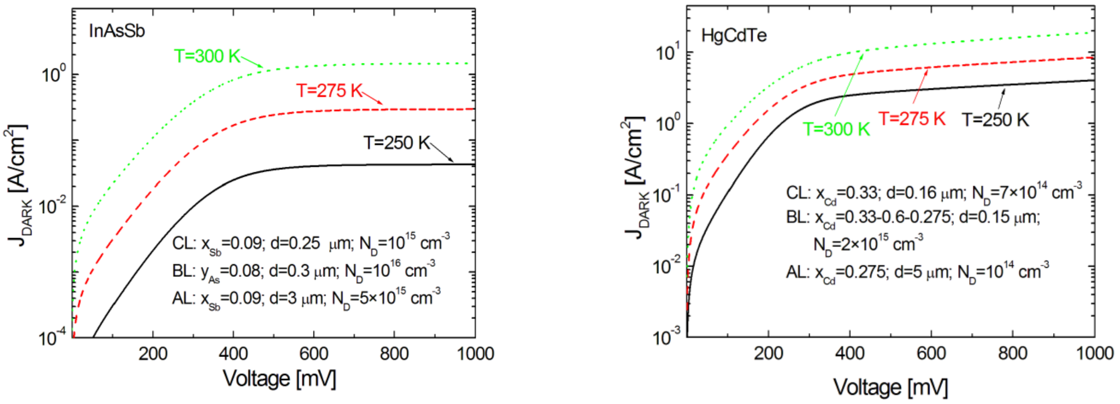

(a) *(b)*

Fig. 8. J_{DARK} versus voltage for nBn InAsSb/B-AlAsSb (a) and HgCdTe/B-HgCdTe (b) detectors for selected temperatures.

As mentioned, introducing of the p-type CL to the barrier structure increases barrier in conduction band and reduces barrier in valence band respectively restricting electron thermionic emission over the ΔE_c and allowing zero-bias operation (low ΔE_v). Fig. 9 (a) and (b) depict J_{DARK} and J_{PHOTO} (calculated for λ = 3.3 μm) for InAsSb/B-AlAsSb detector for selected CL doping (p/n-type $10^{15}/10^{17}$ cm^{-3}). Comparing the nBn and pBn structures for the same level but opposite doping $N_D = N_A = 10^{15}$ cm^{-3}, both J_{DARK} and J_{PHOTO} are comparable. The situation changes for high doping (10^{17} cm^{-3}) when J_{DARK} for nBn structure is lower nearly two orders of magnitude in comparison to pBn but at the same time photocurrent is proportionally higher and favours p-type CL (see Fig. 9 (b)). This behaviour is directly related to the ΔE_c and ΔE_v dependence on bias, where for V = 400 mV, ΔE_v = 120→40 meV and ΔE_c = 2044→2035 meV (see Fig. 6 (a) and (b)).

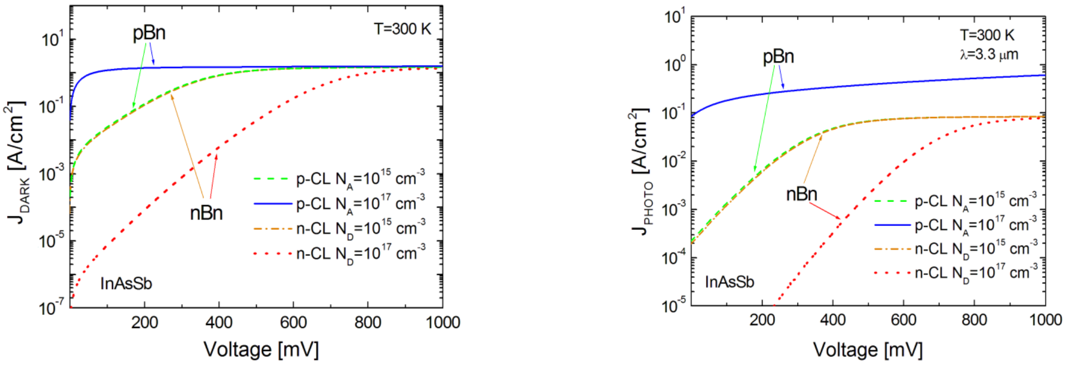

(a) *(b)*

Fig. 9. J_{DARK} (a) and J_{PHOTO} (b) versus voltage for nBn and pBn InAsSb/B-AlAsSb detectors for selected CL doping.

Similar considerations were performed for HgCdTe/B-HgCdTe XBn detectors. In voltage range V = 0→200 mV for $N_D = N_A = 7\times10^{14}$ cm^{-3}, J_{DARK} for pBn is slightly higher in comparison to the nBn architecture which indicates that band offsets in conduction and valence bands are comparable for both nBn and pBn architectures. Both ΔE_c and ΔE_v voltage dependence is clearly evident in Fig. 10 (a) and (b), where for V = 400 mV, ΔE_v = 45→30 meV and ΔE_c = 330→240 meV.

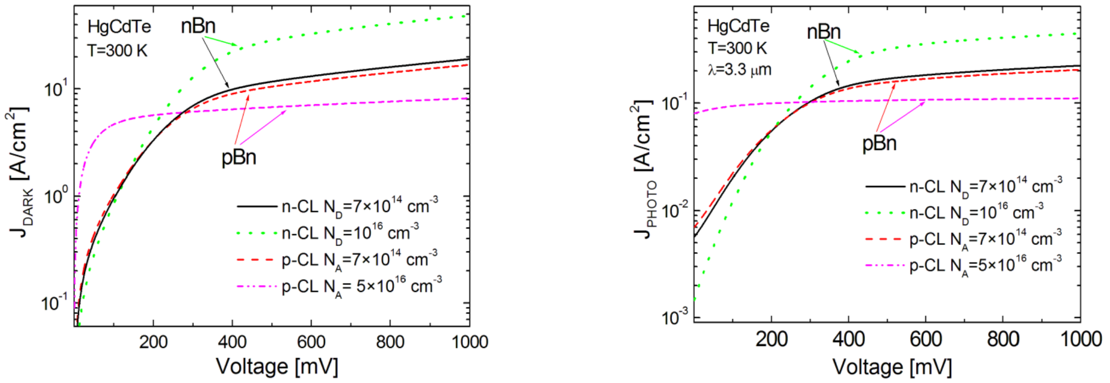

(a) *(b)*

Fig. 10. J_{DARK} (a) and J_{PHOTO} (b) versus voltage for nBn and pBn HgCdTe/B-HgCdTe detectors for selected CL doping.

Fig. 11 (a) compares D^* versus CL doping level for HgCdTe/B-HgCdTe material system. The maximum detectivity for both XBn detectors was estimated at the level ~ 10^9 cmHz$^{1/2}$/W. For analyzed structure the spectacular improvement of the detectivity is not observed for pBn detector (assuming BL $N_D = 2\times10^{15}$ cm^{-3} and AL $N_D = 10^{14}$ cm^{-3}). The p-type CL is advisable only for low doping while CL n-type doping is favorable above 5×10^{15} cm^{-3}. For InAsSb/B-AlAsSb (see Fig. 11 (b)) pBn architecture is better for high CL p-type doping $N_A > 10^{16}$ cm^{-3}, while CL n-type doping allows to reach higher performance below 5×10^{16} cm^{-3} depending on voltage. The maximum D^* for this material system was found to be 7×10^9 cmHz$^{1/2}$/W in analyzed voltage range. It must be stressed that for low voltages, nBn performance is limited by low quantum efficiency. Simulated InAsSb/B-AlAsSb nBn goes to BLIP conditions around $T \approx 185$ K.

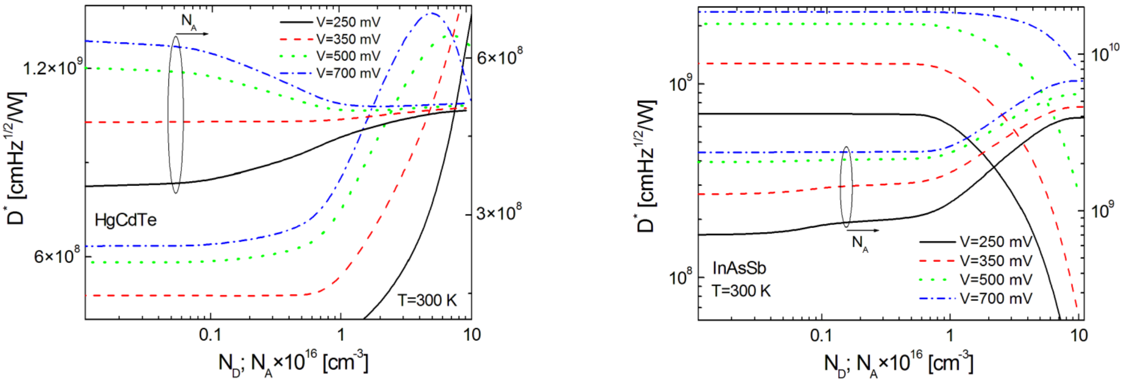

(a) *(b)*

Fig. 11. D^* versus type of CL doping for: HgCdTe/B-HgCdTe (a) and InAsSb/B-AlAsSb (b) detectors.

3. IB CID T2SLs InAs/GaSb structures

The devices presented in this work were fabricated in Center for High Technology Materials, University of New Mexico, Albuquerque. The schematic of a typical T2SLs detector with the IB design intended to operate in the MWIR spectral region is shown in Fig. 12 (a). The detector structure was grown on a GaSb n-type substrate. The first layer of the devices was a 639 nm thick n-type superlattice bottom contact composed of 120 Periods (3P) of 12.5 ML of InAs and 5 ML of AlSb doped with GaTe (N_D = 3×10^{18} cm^{-3}). After, seven stages were grown playing the following role:

a) non intentionally doped (n.i.d) transport/relaxation region consisted of four T2SLs 3P InAs/AlSb sub-layers with increasing InAs's width and decreasing AlSb thickness within the range 12.5 ML→20 ML and 5 ML→4 ML respectively;

b) n.i.d tunnelling region AlSb-barrier (d = 2 nm)/GaSb-well (d = 3.5 nm)/AlSb-barrier (d = 2 nm);

c) residually n-type doped (N_D = 10^{16} cm^{-3}) absorber layer made of 29P T2SLs 9 ML InAs/9 ML GaSb with total thickness d = 153 nm.

Next, seven cascade stages are preceded by transport/relaxation region and 2 nm thick n.i.d AlSb barrier. Finally, the 150 nm thick p-type doped with Be (N_A = 3×10^{18} cm^{-3}) top contact layer was grown. Due to built-in electric field, photo-generated electron-hole pairs in the absorber region move in opposite directions: electrons to the right while the holes to the left. The separation between the quantized energy level in the GaSb quantum well of tunneling region and the valence band in active region is designed to be equal to the LO-phonon energy in AlSb to make the tunnelling of holes a phonon-assisted process. The hole and electron barriers represented by the relaxation region and the interband tunnelling region also act as the hole and electron barriers and block the flow of dark carriers from one cascade stage into the other. Simulated IB CID T2SLs InAs/GaSb energy band diagram is presented in Fig. 12 (b).

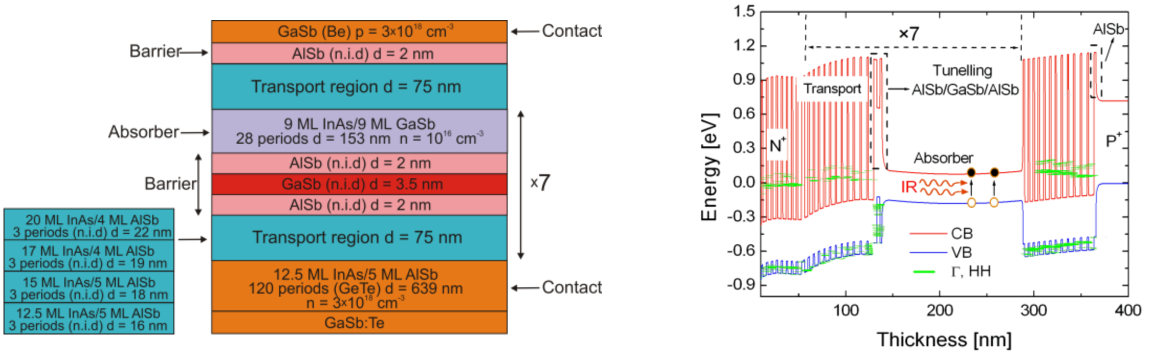

(a) *(b)*

Fig. 12. Schematic illustration of the IB CID T2SLs InAs/GaSb structure photodetector (a); simulated energy band diagram (b).

Fig. 13 (a) presents Arrhenius plot of the dark current versus inverse temperature for selected voltages. Activation energy was estimated to be at the level of $E_a \approx$ 130 meV which corresponds to active layer $E_g/2$. This indicates that dark current is SRH GR driven. In addition, J_{DARK} characteristics versus voltage (forward and reverse bias) are depicted in Fig. 13 (b).

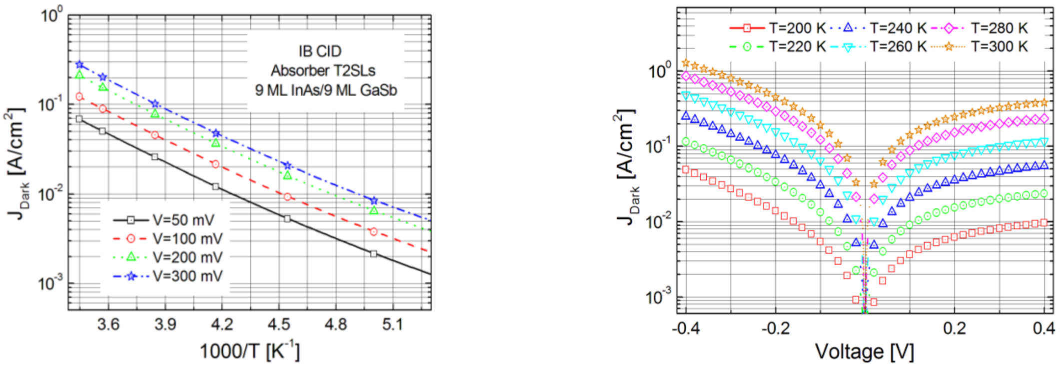

(a) *(b)*

Fig. 13. Arrhenius plot of the dark current density versus inverse temperature (a); J_{DARK} versus voltage for selected temperatures (b) for IB CID T2SLs InAs/GaSb.

Fig. 14 (a) shows the dependence of T2SLs InAs/GaSb active layer E_g on temperature. The fitting curve (solid line) is plotted using the well-known Varshni's equation. The fitting parameters in linearquadratic Varshni relation were assumed to be equal $E_g(0) = 0.285$ eV, $\beta = 270$ K and $\alpha = 3.1\times10^{-4}$ eVK^{-1} [28].

Simulated J_{DARK} at T = 200 K versus voltage are presented in Fig.14 (b). The characteristic parameters used in simulation: MFP (*mean free path*) and BRC (*bulk radiative coefficient; effective spontaneous emission coefficient for* SLs) were assumed at the level MFP = 0.3/1 µm and BRC = 2×10^{-17} m^3/s. The detailed description of the model could be found in the paper by Li *et al.* [29].

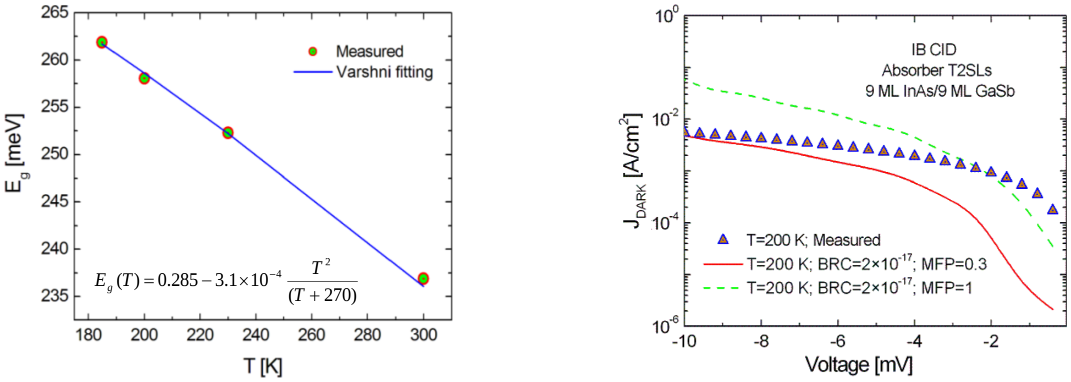

(a) *(b)*

Fig. 14. Varshni E_g temperature dependence for active layer (a); simulated J_{DARK} versus voltage for IB CID T2SLs InAs/GaSb photodetector (b).

The spectral responsivity of MWIR T2SL InAs/GaSb cascade detector with 7-µm cut-off wavelength has been observed up to 420 K at bias voltage of 0.5 V. At room temperature and at wavelength ≈ 4 µm, the Johnson noise limited detectivity is 9×10^8 cmHz$^{1/2}$/W [30]. The performance of the device can further be improved by the doping optimization in the absorber and barrier regions. The zero bias spectral response characteristics and detectivity versus wavelength for selected temperatures are preseted in Fig. 15 (a) and (b) respectively.

Even though, IB CID quantum efficiency is low (typically below 10%), it is predicted that with a better understanding of the quantum cascade device physics and other aspects related to their design and material properties the high performance HOT detectors will be fabricated.

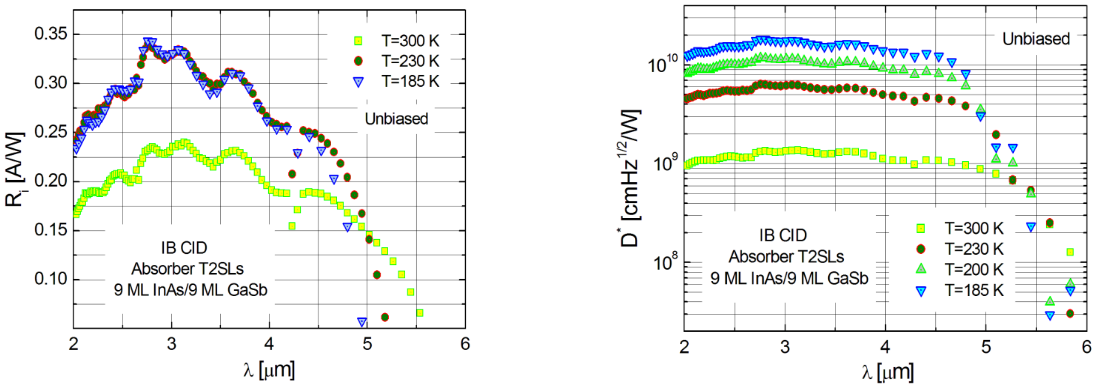

(a) *(b)*

Fig. 15. Spectral response for selected temperatures (a); D^* versus wavelength for IB CID T2SLs InAs/GaSb photodetector (b).

4. Comparison of the IR technologies

Fig. 16 shows the performance of the HgCdTe, InAsSb and T2SLs InAs/GaSb HOT detectors. Without optical immersion MWIR photovoltaic detectors are sub-BLIP devices with performance close to the generation-recombination limit, but well designed optically immersed devices approach BLIP (calculated for 2π FOV) limit when thermoelectrically (TE) cooled with 2-stage Peltier coolers.

The spectral detectivity for nBn T2SLs InAs/GaSb (10 ML/10 ML) and B-Al$_{0.2}$Ga$_{0.8}$Sb was presented for T = 300 K. The maximum $D^* = 4\times10^8$ cmHz$^{1/2}$/W and quantum efficiency 15% [15]. Improvement of T2SLs uniformity in the size of the constituent layers should lead to higher performance. nBn and CBIRD HgCdTe detectors operating in the MWIR range at T = 200 K reaches 6×10^9 and 2×10^{10} cmHz$^{1/2}$/W respectively. Additional barrier in CBIRD HgCdTe structure increases detectivity almost 10 times [26].

The most promising are IB CID detectors. The IB CID experimental results were taken after Tian *et al.*, Yang *et al.* and Gautam *et al*. [17,30−32]. These detectors combine the advantages of interband optical transitions with the excellent carrier transport properties of the interband cascade laser structures. Thermal generation rate at any specific temperature and cut-off wavelength in these devices is usually orders of magnitude smaller than for corresponding intersubband quantum cascade infrared detectors (IC QCIDs). The IC QCID experimental results were presented after Hofstetter *et al*. [33].

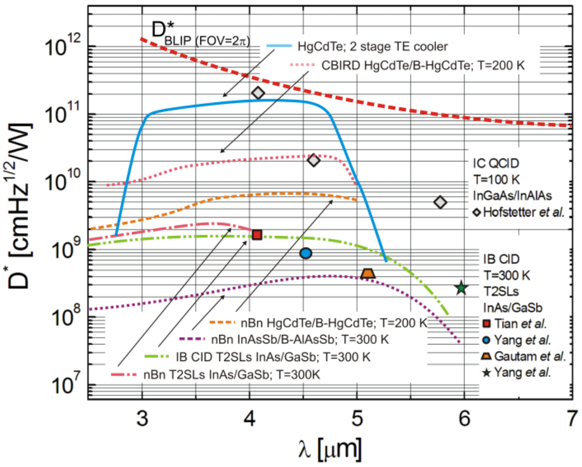

Fig. 16. Spectral detectivity as a function of wavelength for different types of CIDs; nBn T2SLs InAs/GaSb (T = 300 K); nBn InAsSb/B-AlAsSb (T = 300 K); nBn HgCdTe/B-HgCdTe (T = 200 K); CBIRD HgCdTe (T = 200 K) and HgCdTe detectors with 2-stage TE coolers.

5. Conclusions

In the case of infrared HOT photodetectors several new strategies have been introduced including barrier detectors and interband cascade detectors. Especially, more promising are IB CIDs with T2SLs InAs/GaSb active layers. At present stage of technology, their experimentally measured spectral response at room temperature are higher than those predicted for HgCdTe photodiodes. Improvement of their design may allow achieving higher performance.

The XBn detectors exhibit their capability below crossover temperature. Unbiased operation could be reached by implementing of p-type CL to the detector structure. This solution is suggested for the materials exhibiting low conduction band offset.

Acknowledgments

We acknowledge support by Department of Electrical and Computer Engineering, Center for High Technology Materials, University of New Mexico, Albuquerque. This paper has been done under financial support of the Polish National Science Centre, Project:**UMO-2012/07/D/ST7/02564** and the Polish Ministry of Sciences and Higher Education, Key Project: **POIG.01.03.01-14-016/08** "New Photonic Materials and their Advanced Application".

References

[1] A. Rogalski, CRC Press, Boca Raton, 2011.
[2] J. Piotrowski, A. Rogalski, Infrared Phys. Technol. **46**, 115 (2004).
[3] J. Piotrowski, A. Rogalski, in Narrow-Gap II–VI Compounds and Electromagnetic Applications, ed. by P. Capper Chapman & Hall, London, 1997.
[4] C. T. Elliott, Semicond. Sci. Technol. **5**, S30 (1990).
[5] H. Kocer, Solid-State Electron. **87**, 58 (2013).
[6] P. Martyniuk, A. Rogalski, Proc. SPIE **6940**, 694004 (2008).
[7] S. Maimon, G. Wicks, Appl. Phys. Lett. **89**, 151109 (2006).
[8] E. H. Aifer, J. G. Tischler, J. H. Warner, I. Vurgaftman, J. C. Kim, J. R. Meyer, B. R. Bennett, L. J. Whitman, Proc. SPIE **5732**, 259 (2005).
[9] B. M. Nguyen, D. Hoffman, P. Y. Delaunay, M. Razeghi, Appl. Phys. Lett. **91**, 163511 (2007).
[10] O. Salihoglu, A. Muti, K. Kutluer, T. Tansel, R. Turan, Appl. Phys. Lett. **101**, 073505 (2012).
[11] D. Z.-Y. Ting, C. J. Hill, A. Soibel, S. A. Keo, J. M. Mumolo, J. Nguyen, S. D. Gunapala, Appl. Phys. Lett. **95**, 023508 (2009).
[12] J. R. Pedrazzani, S. Maimon, G. W. Wicks, Electron. Lett. **44**, 25 (2008).
[13] P. Klipstein, Proc. SPIE **6940**, 69402U-1–11 (2008).
[14] S. Myers, E. Plis, C. Morath, V. Cowan, N. Gautam, B. Klein, M. N. Kutty, M. Naydenkov, T. Schuler-Sandya, S. Krishna, Proc. SPIE **8155**, 815507-1 (2011).
[15] J. Wróbel, P. Martyniuk, E. Plis, P. Madejczyk, W. Gawron, S. Krishna, A. Rogalski, Proc. SPIE **8353**, 8353-16 (2012).
[16] A. M. Itsuno, J. D. Philips, S. Velicu, J. Elect. Mater. **40**, 1624 (2011).
[17] N. Gautam, S. Myers, A. V. Barve, B. Klein, E. P. Smith, D. R. Rhiger, L. R. Dawson, S. Krishna, Appl. Phys. Lett. **101**, 021106-1–4 (2012).
[18] G. R. Savich, J. R. Pedrazzani, D. E. Sidor, S. Maimon, G. W. Wicks, Appl. Phys. Lett. **99**, 121112 (2011).
[19] G. R. Savich, J. R. Pedrazzani, D. E. Sidor, G. W. Wicks, Infrared Phys. Technol. **48**, 39 (2013).
[20] E. Weiss, O. Klin, S. Grossmann, N. Snapi, I. Lukomsky, D. Aronov, M. Yassen, E. Berkowitz, A. Glozman, P. Klipstein, A. Freankel, I. Shtrichman, J. Cryst. Growth **339**, 31 (2012).
[21] A. M. Itsuno, J. D. Philips, S. Velicu, Appl. Phys. Lett. **100**, 161102 (2012).
[22] B. V. Shanabrook, W. Barvosa-Carter, R. Bass, B. R. Bennett, J. B. Boos, W. Bewley, A. S. Bracker, J. C. Culberston, E. R. Glaser, W. Kruppa, R. Magno, W. J. Moore, J. R. Meyer, B. Z. Nosho, D. Park, P. M. Thibado, M. E. Twigg, R. J. Wagner, J. R. Waterman, L. J. Whtman, M. J. Yang, Proc. SPIE **3790** (1999).

[23] G. J. Brown, Proc. SPIE **5783** (2005).

[24] D. Z.-Y. Ting, A. Soibel, L. Höglund, J. Nguyen, C. J. Hill, A. Khoshakhlagh, S. D. Gunapala, in Semiconductors and Semimetals, ed. by S. D. Gunapala, D. R. Rhiger, C. Jagadish, Elsevier, Amsterdam, p. 1, 2011.

[25] F. Klem, S. D. Hawkins, J. K. Kim, D. Leonhardt, E. A. Shaner, J. Vac. Sci. Technol. **B 31**, 3 (2013).

[26] P. Martyniuk, A. Rogalski, Solid-State Electron. **80,** 96 (2013).

[27] P. Martyniuk, A. Rogalski, Proc. SPIE **8704**, 87041X (2013).

[28] B. Klein, E. Plis, M.N. Kutty, N. Gautam, A. Albrecht, S. Myers, S. Krishna, J. Phys. D: Appl. Phys. **44**, 075102-1–5 (2011).

[29] Z. Li, Y. Y. Li, G. P. Ru, J. Appl. Phys. **110**, 093109 (2011).

[30] J. V. Li, R. Q. Yang, C. J. Hill, S. L. Chung, Appl. Phys. Lett. **86**, 101102-1–3 (2005).

[31] R. Q. Yang, Z. Tian, Z. Cai, J. F. Klem, M. B. Johnson, H. C. Liu, J. Appl. Phys. **107**, 054514-1–6 (2010).

[32] Z. Tian, R. T. Hinkey, R. Q. Yang, D. Lubyshev, Y. Qiu, J. M. Fastenau, W. K. Liu, M. B. Johnson, J. Appl. Phys. **111**, 024510-1–6 (2012).

[33] D. Hofstetter, F. R. Giorgetta, E. Baumann, Q. Yang, C. Manz, K. Köhler, Appl. Phys. **B 100**, 313 (2010).

---

[*] Corresponding author: pmartyniuk@wat.edu.pl